2015

Green Bank Telescope And Swift X-Ray Telescope Observations Of The Galactic Center Radio Magnetar Sgr J1745–2900

Ryan S. Lynch

Robert F. Archibald

Victoria M. Kaspi

Paul Scholz

The Astrophysical Journal, 806:266 (10pp), 2015 June 20 doi:10.1088/0004-637X/806/2/266

GREEN BANK TELESCOPE AND *SWIFT* X-RAY TELESCOPE OBSERVATIONS OF THE GALACTIC CENTER RADIO MAGNETAR SGR J1745–2900

Ryan S. Lynch[1,2,3], Robert F. Archibald[1], Victoria M. Kaspi[1], and Paul Scholz[1]
[1] Department of Physics, McGill University, 3600 University Street, Montreal, Quebec, H3A 2T8, Canada
[2] National Radio Astronomy Observatory, P.O. Box 2, Green Bank, West Virginia, 24944, USA
[3] Department of Physics and Astronomy, West Virginia University, P.O. Box 6315, Morgantown, WV 26506, USA; rlynch@physics.mcgill.ca
Received 2014 December 1; accepted 2015 May 6; published 2015 June 23

ABSTRACT

We present results from eight months of Green Bank Telescope 8.7 GHz observations and nearly 18 months of *Swift* X-ray telescope observations of the radio magnetar SGR J1745–2900. We tracked the radio and X-ray flux density, polarization properties, profile evolution, rotation, and single-pulse behavior. We identified two main periods of activity. The first is characterized by approximately 5.5 months of relatively stable evolution in radio flux density, rotation, and profile shape, while in the second these properties varied substantially. Specifically, a third profile component emerged and the radio flux also became more variable. The single pulse properties also changed, most notably with a larger fraction of pulses with pulse widths ∼5–20 ms in the erratic state. Bright single pulses are well described by a log-normal energy distribution at low energies, but with an excess at high energies. The 2–10 keV flux decayed steadily since the initial X-ray outburst, while the radio flux remained stable to within ∼20% during the stable state. A joint pulsar timing analysis of the radio and X-ray data shows a level of timing noise unprecedented in a radio magnetar, though during the time covered by the radio data alone the timing noise was at a level similar to that observed in other radio magnetars. While SGR J1745–2900 is similar to other radio magnetars in many regards, it differs by having experienced a period of relative stability in the radio that now appears to have ended, while the X-ray properties evolved independently.

Key words: pulsars: individual (SGR J1745–2900) – stars: magnetars

1. INTRODUCTION

Magnetars are neutron stars that display intense short X-ray bursts, X-ray pulsations, and X-ray outbursts that are typically followed by a decaying X-ray flux. The hallmark of magnetar activity is an X-ray luminosity that may exceed the power available from the neutron star's rotation. Instead, magnetars are believed to be powered by the decay of their enormous internal magnetic fields (Thompson & Duncan 1995, 1996; Thompson et al. 2002; Beloborodov 2009), and the most active magnetars[4] generally have inferred surface dipolar magnetic fields of 10^{14}–10^{15} G, much higher than the $\sim 10^{12}$ G typical of rotation-powered radio pulsars. Under this interpretation, as the internal magnetic field decays, it stresses the stellar crust, inducing occasional sudden crustal and/or magnetospheric reconfigurations that give rise to the variety of variable X-ray emission.

Pulsed radio emission has been detected from four magnetars thus far (Camilo et al. 2006, 2007a; Levin et al. 2010; Eatough et al. 2013b; Shannon & Johnston 2013). Their radio properties show both similarities and marked differences when compared to those of rotation-powered pulsars. Like all magnetars (e.g., Dib & Kaspi 2014), the four radio magnetars have a high degree of timing noise and experience significant changes in torque (e.g., Camilo et al. 2007c). Both rotation-powered pulsars and radio magnetars exhibit a high degree of linear polarization (Camilo et al. 2007a, 2007b; Kramer et al. 2007; Levin et al. 2012; Eatough et al. 2013b; Shannon & Johnston 2013) and have radio spectra that can be well modeled with a single power law, $S_\nu \propto \nu^\alpha$. However, magnetars have shallow or even flat spectra, with α that may vary significantly with time (e.g., Camilo et al. 2007d), whereas rotation-powered pulsars typically have stable spectra with $\langle\alpha\rangle \sim -1.6$ (Bates et al. 2013). The flux density and pulse profile morphology of some radio magnetars are also highly variable (e.g., Camilo et al. 2007c). This may be due, at least in part, to the emission of erratic, extremely narrow single pulses and very long profile stabilization timescales (Kramer et al. 2007). Single pulse studies of magnetars have not revealed evidence for drifting sub-pulses of the kind sometimes seen in rotation-powered pulsars (Serylak et al. 2009).

The newest of the four known radio magnetars is SGR J1745–2900.[5] The X-ray source was discovered in outburst by Kennea et al. (2013c) using *Swift*. Subsequent observations with the *NuSTAR* X-ray telescope detected pulsations with a spin period $P = 3.76$ s and $\dot{P} = 6.5 \times 10^{-12}$ s s^{-1}, implying a magnetic field of strength $B = 1.6 \times 10^{14}$ G, thus confirming the pulsar's nature as a magnetar (Mori et al. 2013). Radio pulsations at the same period were subsequently detected at several observatories (Eatough et al. 2013b; Shannon & Johnston 2013). SGR J1745–2900 lies only 2.″4 in projection from Sgr A* (Rea et al. 2013), and its dispersion measure (DM = 1778 ± 3 pc cm^{-3}) suggests that the source lies <10 pc from Sgr A* itself (Eatough et al. 2013b). Early radio observations have measured a flat spectrum and high degree of polarized emission for SGR J1745–2900, much like in other radio magnetars (Eatough et al. 2013a; Shannon & Johnston 2013).

Here, we report on the results from an observing campaign of SGR J1745–2900 using the Robert C. Byrd Green Bank Telescope (GBT), supplemented with data from the *Swift*

[4] For an up-to-date list of known magnetars see the McGill magnetar catalog at http://www.physics.mcgill.ca/~pulsar/magnetar/main.html (Olausen & Kaspi 2014).

[5] Olausen & Kaspi (2014) also refer to this source as MG J1745–2900.

X-ray Telescope (XRT) and *NuSTAR* telescope. We tracked the evolution of the spin, radio flux density, polarization, and profile morphology of the pulsar at 8.7 GHz, and have also analyzed properties of its single pulses. XRT was used to measure the 2–10 keV flux. We first provide relevant background on the magnetar's behavior in Section 2. In Section 3 we describe our observational set-up and data reduction. Our analysis and results are presented in Section 4, and discussed in more detail in Section 5.

2. OVERVIEW OF RADIO AND X-RAY BEHAVIOR

Before we discuss our results in detail, we provide some context by highlighting some of the radio and X-ray properties of SGR J1745–2900 reported elsewhere. Radio pulse profiles obtained shortly after the magnetar was first detected had a single Gaussian component from ∼1.2 to 19 GHz (Shannon & Johnston 2013; Spitler et al. 2014b), though there appears to be visual hints of a second profile component emerging in some of the profiles presented by Eatough et al. (2013b). The early reported flux densities near 9 GHz varied but were of order ∼1 mJy.

After the initial outburst, the X-ray flux of SGR J1745–2900 began to decay. The *Swift* Burst Alert Telescope (BAT) detected short bursts on MJDs 56407 (2013 April 25; Kennea et al. 2013d), 56450 (2013 June 7; Kennea et al. 2013a), and 56509 (2013 August 5; Kennea et al. 2013b). Another possible burst was detected with *INTEGRAL* on MJD 56555[6] (2013 September 20; Mereghetti et al. 2013). Despite this, the overall flux decay continued. Kaspi et al. (2014) suggested that the burst on MJD 56450 may have been accompanied by a change in spin-down ($\dot{f}$), though there was no discontinuity in spin frequency. This behavior was not consistent with a glitch or anti-glitch, though timing noise could not be ruled out.

Yusef-Zadeh et al. (2014) observed SGR J1745–2900 on 2014 February 25 (MJD 56713) at 44 GHz with the Very Large Array and measured a flux density that was ∼20 times higher than an upper limit obtained in 2011 August at the same frequency. *Chandra* observations at the same epoch as Yusef-Zadeh et al. (2014) showed no evidence of a corresponding increase in X-ray flux when compared to surrounding epochs in 2014 (Rea et al. 2014). We observed SGR J1745–2900 31 days prior to and 13 days after this 44 GHz flux density increase (on MJDs 56682 and 56726, respectively). As discussed below, our data provide evidence that SGR J1745–2900 underwent a change in flux density, pulse profile morphology, and possibly rotational parameters sometime between the above two observations, changing from a fairly stable state to a more erratic radio state. We will refer to the stable state (covering MJDs 56515–56682) and erratic state (covering MJDs 56726–56845) throughout. We will discuss the extent to which we can associate this state change with the 44 GHz radio brightening in Section 5.

3. OBSERVATIONS AND DATA REDUCTION

3.1. GBT

We observed SGR J1745–2900 in 33 epochs. We used an approximately weekly cadence from 2013 August 11 through 2014 January 25,[7] during which integration times averaged about 30 minutes. Because SGR J1745–2900 was fairly stable over this period, we planned on switching to a monthly cadence with two hour integrations starting in 2014 February. However, after two monthly monitoring sessions, it became apparent that the magnetar had increased in variability. Therefore, we reallocated our time to allow for more frequent but shorter, 30 minute observations, though scheduling constraints prevented us from restarting weekly sessions.

We used the X-band receiver system of the GBT at a center frequency $\nu_c = 8.7$ GHz and with an instantaneous bandwidth of $\Delta\nu = 800$ MHz, recording dual circular polarizations. The data were recorded with the the Green Bank Ultimate Pulsar Processing Instrument, using 512 frequency channels and a sampling time of $\delta t = 163.84\ \mu$s. At the beginning of each observing session we took on- and off-source scans of a standard flux calibrator while firing the GBT pulsed noise diode. We initially used 3C353 as a flux standard, but after noticing anomalies in the flux densities we calculated, we switched to using 3C286 on and after 2014 May 12 (see Section 4.1 for a detailed discussion of our reported flux density measurements). We observed the noise diode again at the position of SGR J1745–2900 before observing the magnetar, and used these data for calibration purposes.

The data were folded modulo the rotational period of SGR J1745–2900, using 1024 bins in pulse phase and sub-integrations with a duration of one rotation, thus preserving information on individual single pulses. Radio frequency interference (RFI) was usually minimal, but when present we excised it manually by explicitly removing contaminated frequency channels and sub-integrations. We also removed ∼2.5% from the top and bottom of the frequency band due to roll-off in the receiver sensitivity. This was usually sufficient for obtaining integrated pulse profiles with few artifacts, but on certain epochs significant fluctuations in the off-pulse region were evident (as an example, see the profile from MJD 56677 in Figure 1). The effect is usually (though not exclusively) associated with observations that occurred at elevation angles below ∼10°, and we believe that they are primarily caused by changes in atmospheric opacity. To ensure that the fluctuations are not intrinsic to SGR J1745–2900, we folded the data at a period randomly drawn from a uniform distribution on an interval $P \pm 0.5$ s, where $P = 3.76$ s is the spin period of the magnetar. This effectively allowed us to sample the period space around the magnetar while avoiding bias in the chosen period. As expected, similar fluctuations were readily apparent when folding at the randomly selected period, demonstrating that they are extrinsic to SGR J1745–2900.

After folding and RFI excision, the total, linearly, and circularly polarized flux densities were calibrated using standard routines from the `PSRCHIVE` software package (Hotan et al. 2004). On- and off-source observations of the standard flux calibrator were used to measure the absolute flux density of the pulsed noise diode, and this in turn was used to calibrate the total and polarized flux density of SGR J1745–2900. We corrected for Faraday rotation by searching over a range of rotation measures (RMs; again using `PSRCHIVE` standard tools), from $-2 \times 10^5 \leqslant \mathrm{RM} \leqslant 0$ rad m^{-2}, de-rotating our data at the RM that maximized the linearly polarized flux density. All subsequent analyses were performed on these calibrated, RM-corrected data unless otherwise noted.

[6] This burst occurred approximately 12 hr after one of our GBT observations, but there is nothing abnormal about the radio properties at this epoch.

[7] No observations were possible from 2013 October 4 to 18 because GBT operations were suspended due the U.S. Federal Government shutdown.

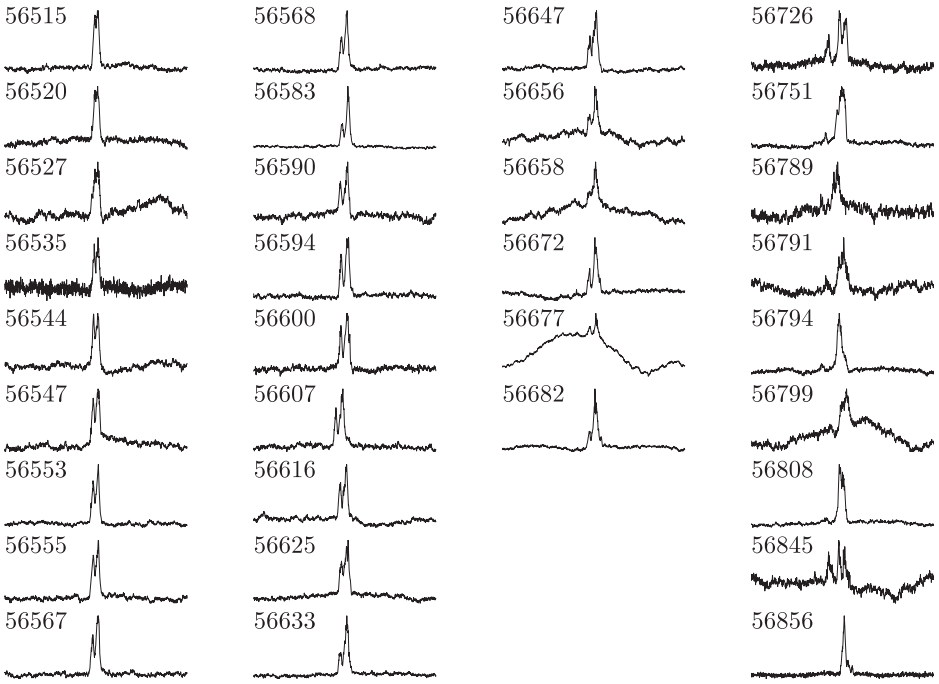

Figure 1. Integrated 8.7 GHz pules profiles of SGR J1745–2900 at each of our observing epochs, which are indicated by MJD. For clarity, profiles are centered and scaled to have the same peak amplitude. As described in the text, baseline fluctuations that we attribute to changes in atmospheric opacity are evident at certain epochs and are not intrinsic to SGR J1745–2900. Up to MJD 56682 (first three columns), the profile shape was fairly stable, exhibiting a clear double peaked structure. Changes in the relative amplitude of the two peaks are most likely due to the pulse-to-pulse variability, given the relatively small number of rotations observed at each epoch, which prevents the profile from fully stabilizing. Starting with MJD 56726 (fourth column), the profile became more variable, often showing a third component.

3.2. Swift *XRT*

In order to characterize the X-ray flux evolution of SGR J1745–2900, we analyzed 416 *Swift* XRT observations of the source obtained between MJDs 56407 and 56956 as part of the Galactic center monitoring program (Degenaar et al. 2013). Observations were typically 1 ks long and occurred nearly daily, except between MJDs 56599 and 56690, when the source was in Sun-constraint. A total of ∼438 ks of data were analyzed.

The XRT (Burrows et al. 2005) is a Wolter-I telescope with an *XMM-Newton* EPIC-MOS CCD22 detector, sensitive in the 0.5–10 keV range. For all the observations presented here, the XRT was operated in Photon Counting (PC) mode, which has a time resolution of 2.5 s. We obtained Level-1 data products from the HEASARC *Swift* archive, reduced them using the *xrtpipeline* standard reduction script, and transformed them, using HEASOFT v6.16, to the solar system barycenter using the *Chandra* position (Rea et al. 2013) of SGR J1745–2900. Individual exposure maps, spectra, and ancillary response files were created for each orbit and then summed.

4. ANALYSIS

4.1. Radio Flux and Polarization Properties

We began the process of measuring the mean flux density, S_ν, of SGR J1745–2900 by systematically identifying the on-pulse region at each epoch. This was done by selecting the profile bins to both the left and right of the profile peak at which the flux density reached the rms level of the integrated profile as a whole. This gave us a rough idea of the on-pulse and off-pulse bins. We iterated this procedure using the rms of the updated off-pulse region until the results converged. The baseline fluctuations described in Section 3 may bias this procedure in two ways—by raising the off-pulse rms and by making the on-pulse region appear broader than it actually is. We attempted to mitigate this by fitting a third order polynomial to the integrated profile (but using only the off-pulse region) and subtracting it to flatten the baseline. We used this approach to determine the on-pulse region, but used the original, unflattened profile to calculate S_ν.

We found that, when using 3C353 as flux calibrator, our calculated 8.7 GHz flux densities were consistently a factor of ∼10–20 higher than those reported by Shannon & Johnston (2013) and Eatough et al. (2013b) at similar frequencies. To confirm this discrepancy we observed both 3C353 and 3C286 on the same date, and calibrated our data from that date independently using both sources. The data calibrated using 3C286 were in rough agreement with the two previous reports of $S_{8.7\,\mathrm{GHz}}$ (which we note were obtained independently from each other with different telescopes), while the data calibrated using 3C 353 were a factor of several higher. From this, we concluded that 3C 353 is not a reliable flux standard at these frequencies. We subsequently used only 3C286 for flux calibration, observing it at a total of five epochs, though a hardware error made one of these unusable for flux calibration. To measure the flux density at all of our observing epochs, we independently calibrated all of our data using the four reliable 3C286 observations. This resulted in four separate flux measurements at each of our 33 observing epochs, although three epochs had to be discarded from the flux density analysis because of malfunctions of the noise diode. Even though we used the same flux standard, there was still scatter among these four flux density values. The flux density we report here is the mean of these and the uncertainties represent the minimum and

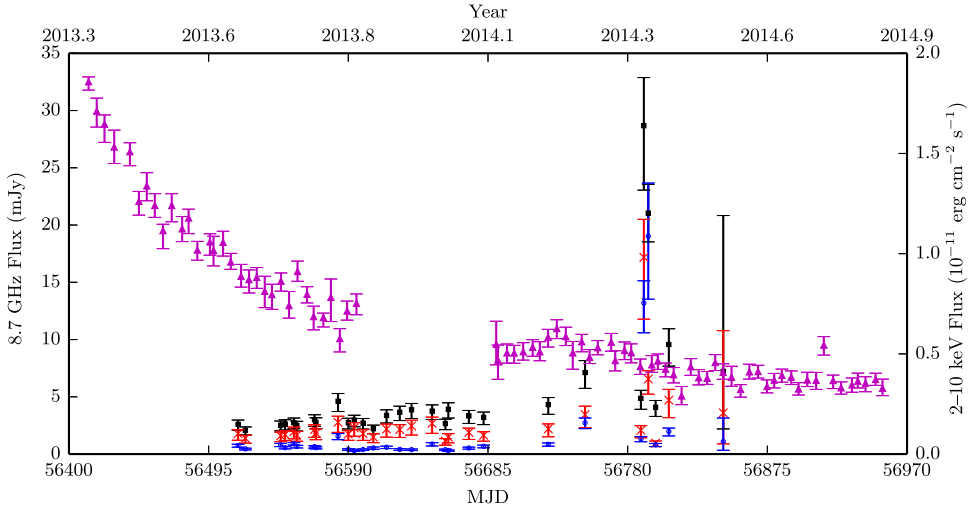

Figure 2. Period-averaged 8.7 GHz flux density and 2–10 keV flux of SGR J1745–2900. The squares (black), crosses (red), and circles (blue) indicate total, linearly polarized, and circularly polarized radio flux density, respectively. X-ray fluxes are indicated by triangles (magenta). Within the uncertainties in our measurements, the radio flux was relatively stable up to MJD 56682, with a mean of ∼3 mJy. After MJD 56726, the flux was more erratic. The X-ray flux has decayed steadily since the initial outburst and is well modeled by a double exponential function (see text for parameters). The moderate X-ray flux increase around MJD 56731 is associated with another source. The X-ray flare on MJD 56910 is most likely associated with Sgr A*.

maximum of the four independent flux density values. Our experience highlights the inherent difficultly of obtaining reliable absolute flux density measurements and can hopefully serve as a cautionary tale to other observers.

The radio flux density is shown in Figure 2 (along with the X-ray flux), while the fractional polarization is shown in Figure 3. During the previously identified stable state (see Section 2), the flux density of SGR J1745–2900 was nearly constant, with a mean $S_{8.7\,\mathrm{GHz}} \approx 3.0$ mJy and a standard deviation of 0.62 mJy between measurements. For comparison, the mean uncertainty in our measurements of $S_{8.7\,\mathrm{GHz}}$ during this state was $^{+0.6}_{-0.4}$ mJy. Like other authors (Eatough et al. 2013b; Shannon & Johnston 2013), we also measure a high degree of linear polarization. The mean linear polarization fraction in the stable state was 0.6, with a standard deviation of 0.09. The circular polariziation was much smaller at 0.2 and with a standard deviation of 0.08.

During the erratic state, the flux of SGR J1745–2900 was both higher and more variable. The mean flux was $S_{8.7\,\mathrm{GHz}} \approx 11$ mJy but with a standard deviation of 8.5 mJy and mean uncertainties of $^{+3.1}_{-2.4}$ mJy. Not only was the standard deviation in $S_{8.7\,\mathrm{GHz}}$ a substantial fraction of the mean (0.78), it was much larger than the uncertainties. The circular polarization fraction increased slightly, with a mean of 0.4 and standard deviation of 0.2, while the linear polarization fraction decreased to a mean of 0.4 with standard deviation of 0.1.

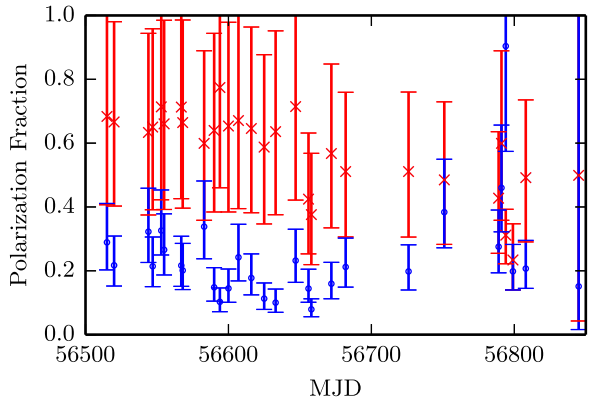

Figure 3. Fraction of linear and circular polarization. Crosses (red) and circles (blue) indicate linear and circular polarization, respectively. During the stable state the linear polarization fraction was relatively constant at ∼0.6, though the uncertainties are large. The circular polarization fraction was typically ∼0.2. During the erratic state, the circular polarization fraction increased to a mean of ∼0.4 while the linear polarization fraction decreased to a mean of ∼0.4.

4.2. X-Ray Flux

To investigate the X-ray flux and spectral behavior, we extracted a circular region centered on SGR J1745–2900 and with a diameter of a 20″, chosen to match the half-power diameter of the XRT at 4 keV. An annulus of inner radius 20″ and outer radius 60″ centered on the source was used to extract background spectra. This is the same background region used by Kennea et al. (2013c). As the angular distance between SGR J1745–2900 and Sgr A* is 2.″4 ± 0.″3, we note that our source region also contains Sgr A*. We summed the spectra in five-day intervals, and grouped them to have a minimum of three counts per bin. Photoelectric absorption was modeled using `XSPEC tbabs`, with abundances from Wilms et al. (2000) and photoelectric cross-sections from Verner et al. (1996). We then fit the spectra to a photoelectrically absorbed blackbody using the "lstat" statistic. The spectra were fit jointly, with a single neutral hydrogen column density (N_{H}) and temperature (kT), allowing only the blackbody normalization to vary for each spectrum. A variable kT was not statistically warranted. This gave best-fit values of $N_{\mathrm{H}} = (12.1 \pm 0.3) \times 10^{22}$ cm^{-2} and $kT = 1.00 \pm 0.01$ keV ($\chi^2 = 8585$ for 8917 degrees of freedom (dof), or lstat = 8620.68). These values of N_{H} and kT are consistent with those reported by Kennea et al. (2013c).

The evolution of 2–10 keV flux is shown alongside $S_{8.7\,\mathrm{GHz}}$ in Figure 2. The flux decay is reasonably well fit ($\chi^2 = 92.6$

for 76 dof) by the sum of two exponential decay functions:

$$F = \Big[\Big(1.00 \pm 0.06\Big)e^{-(t-t_0)/(55\pm7\ \mathrm{d})} + \Big(0.98 \pm 0.07\Big)e^{-(t-t_0)/(500\pm41\ \mathrm{d})}\Big] \times 10^{-11}\ \mathrm{erg\ cm^{-2}\ s^{-1}}, \quad (1)$$

where $t_0 = 56406$ is the the peak of the outburst. There is is a small flux increase around MJD 56731 due to a nearby source leaking into the extraction region, and is not related to the magnetar. There is also a flare evident on MJD 56910 that is likely due to Sgr A* (Degenaar et al. 2014). We see no significant change in the 2–10 keV flux coincident with onset of erratic radio behavior.

4.3. Radio Profile Shape Evolution

Integrated radio pulse profiles of SGR J1745–2900 are shown in Figure 1 for each of our observing epochs. The profile underwent significant changes over the course of our observations. In our earliest data, the profile appeared double peaked, although the two peaks were not always clearly separated prior to MJD 56544. During this period the profile was well fit using a two-component Gaussian model. The most obvious changes in the profile were variations in the relative amplitude of the two Gaussian components from epoch to epoch, which may be due to pulse-to-pulse variability. However, there were also more subtle, long-term changes in the profile. We characterized these by measuring the full width at 20% peak amplitude (W_{20}) and the separation between the two peaks in the profile (Δ). Each quantity was measured by fitting an analytic, two-component Gaussian model to the on-pulse region. The peak amplitude was measured by finding the global maximum of the fit, and W_{20} was found using a bisection method to determine the phase at which the model crossed the 20% flux level on both the leading and trailing sides of the pulse. To measure Δ we simply calculated the pulse phase corresponding to each profile peak.

Uncertainties were quantified following the method outlined by Ferdman et al. (2013). We randomly removed half the profile bins from the on-pulse region, fit a new Gaussian model, and re-calculated the shape parameters as above. We performed 1000 independent Monte Carlo trials and calculated the mean values and the 68.27% (i.e., 1σ) confidence intervals for each parameter from the resulting distributions. The results of this analysis are shown in Figure 4.

There was an obvious increase in both W_{20} and Δ between MJDs 56544 and 56594. Although there is significant scatter compared to our uncertainties, we fit a linear trend to the data over this span and find a rate of change in both W_{20} of and Δ of $0.08 \pm 0.^{\circ}04\ \mathrm{day^{-1}}$. A linear fit to the data between MJDs 56594 and 56682 is consistent with no steady change in either quantity. Because both W_{20} and Δ changed by the same amount, the increase in pulse width can be attributed solely to an increase in the peak separation.

With the onset of the erratic state, the profile changed dramatically (see Figure 1). Due to these large variations we did not calculate W_{20} and Δ for this period. A third component emerged separated by ~0.1 turns from the centroid of the persistent double-peaked main components. Between MJDs 56726 and 56856 the relative amplitude of this third component varied significantly, from nearly equal to that of the two other components to only barely above the noise level. Furthermore, the primary profile component varied between the previously described double-peaked form and a single, broad shape.

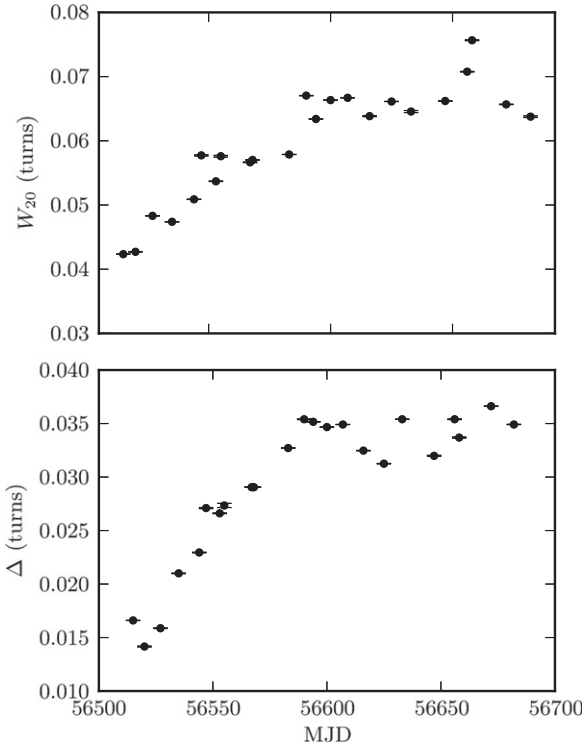

Figure 4. Full width at 20% of peak flux (W_{20}) and peak-to-peak separation (Δ) as a function of time for SGR J1745–2900. Only the stable state is shown. Error bars indicate the 1σ confidence intervals. There is a linear increase in both parameters between MJDs 56544 (2013 September 9) and 56594 (2013 October 29).

4.4. Pulsar Timing

We began the timing analysis of the radio data by fitting a noise-free Gaussian template to a high signal-to-noise ratio (S/N) integrated profile. We used the same template for data obtained during the stable state, i.e., when the magnetar had only two profile components. As noted above, the profile varied from epoch to epoch during this time, which could introduce a bias to our times of arrival (TOAs). However, the profile variations were subtle, with the total change in Δ amounting to only ~0.02 turns, which is of the same order as the rms scatter in our timing residuals and much less than the accumulated phase drift due to timing noise. As such, we are confident that the use of a single template is sufficient for this span of observations. The onset of the erratic state made timing difficult, as discussed below. In all cases, pulse TOAs were calculated via Fourier domain cross-correlation (Taylor 1992) of the templates with the calibrated and RM corrected pulse profiles at each observing epoch. We usually obtained one topocentric TOA per 100 rotations of the magnetar, summing all frequency channels.

We were also able to include previously published TOAs obtained with *Swift* and *NuSTAR* (see Kaspi et al. 2014 for a description of the data set and how these TOAs were obtained). The XRT PC-mode data used to measure 2–10 keV flux lacked the time resolution to measure pulsed emission, hence no TOAs are available from this data set. We allow for an arbitrary phase

Table 1
Timing Parameters of SGR J1745–2900

Data, Statistics, and Assumptions	
Data Span (MJD)	56409–56682
$N_{\rm TOA}$	165
Residual rms (ms)	25.6
Solar System Ephemeris	DE421
Clock Correction Procedure	TT(BIPM12)
Fixed Quantities	
R.A. (J2000)	$17^{\rm h}45^{\rm m}40\overset{\rm s}{.}169$
Decl. (J2000)	$-29°00'29\overset{''}{.}84$
DM (pc cm^{-3})	1778
Reference Epoch (MJD)	56587.0
Measured Quantities	
f (Hz)	0.2656936554(12)
$\dot{f}$ (Hz s^{-1})	$-1.2399(15) \times 10^{-12}$
$\ddot{f}$ (Hz s^{-2})	$-1.047(13) \times 10^{-19}$
$f^{(3)}$ (Hz s^{-3})	$6.7(1.9) \times 10^{-27}$
$f^{(4)}$ (Hz s^{-4})	$3.74(18) \times 10^{-32}$
$f^{(5)}$ (Hz s^{-5})	$-7.1(2.0) \times 10^{-39}$
$f^{(6)}$ (Hz s^{-6})	$-3.90(26) \times 10^{-44}$
$f^{(7)}$ (Hz s^{-7})	$-5.0(1.4) \times 10^{-51}$
$f^{(8)}$ (Hz s^{-8})	$3.34(30) \times 10^{-56}$
$f^{(9)}$ (Hz s^{-9})	$1.83(11) \times 10^{-62}$
$f^{(10)}$ (Hz s^{-10})	$-1.37(17) \times 10^{-68}$
$f^{(11)}$ (Hz s^{-11})	$-1.71(15) \times 10^{-74}$
$f^{(12)}$ (Hz s^{-12})	$-5.05(43) \times 10^{-81}$
Derived Quantities	
$B_{\rm s}$ (G)	$2.6018(16) \times 10^{14}$
$\dot{E}$ (erg s^{-1})	$1.3005(16) \times 10^{34}$
$\tau_{\rm c}$ (year)	3395.2(4.1)

Note. Numbers in parentheses represent 1σ uncertainties in the last digits as determined by TEMPO, scaled such that the reduced χ^2 equals one.

shift between the X-ray TOAs and those obtained with the GBT, which can absorb differences in the profiles, phase offsets between the radio and X-ray emission, DM delays, instrumental shifts, etc. Hence, we cannot determine an absolute phase offset between the radio and X-ray pulses.

TEMPO was used to fit a phase-coherent spin-down model to the radio and X-ray TOAs, making use of the DE421 solar system ephemeris for barycentering and the TT(BIPM12) clock correction chain. We held the coordinates of SGR J1745–2900 fixed at those reported by Rea et al. (2013) and the DM fixed at the valued reported by Eatough et al. (2013b; see Table 1), and hence only fitted for the rotational frequency, f, and its derivatives.

We took our starting solution from Kaspi et al. (2014), which was created using only X-ray observations, and were able to unambiguously phase connect all radio TOAs during the stable state. We found that a simple spin-down model accounting only for f and $\dot{f}$ was insufficient for describing the long-term rotational behavior of SGR J1745–2900 (see the top panel of Figure 5) up to MJD 56682. This is common among magnetars, which exhibit a large degree of timing noise and typically require many higher-order frequency derivatives to accurately model their rotational phase (e.g., Gavriil & Kaspi 2002; Dib & Kaspi 2014). We used twelve frequency derivatives, the maximum allowed by TEMPO, but we caution that this model is not predictive, and is only used to whiten the residuals. Our final solution is presented in Table 1. Fully whitened post-fit residuals are shown in the bottom panel of Figure 5. The reduced χ^2 of our timing solution was large even after fitting all twelve frequency derivatives. To obtain a reduced χ^2 of one, we multiplied the individual TOA errors by a constant error factor, $\epsilon = \sqrt{\chi^2/{\rm dof}} = 6.4$.

Although we could not phase connect all the radio and X-ray TOAs, the solution from Kaspi et al. (2014) was adequate for fitting the combined X-ray/stable radio data set once we included a single, constant phase offset between the two frequencies. Kaspi et al. (2014) reported a possible abrupt change in $\dot{f}$ around MJD 56450, which suggests it was coincident with an X-ray burst. Our results indicate that the suggested change in $\dot{f}$ is consistent with timing noise, and that a second distinct rotational ephemeris is not needed after MJD 56450. It is common to characterize timing noise as the cumulative contribution over the span of observations of the cubic term in the Taylor expansion of the rotational phase (e.g., Arzoumanian et al. 1994):

$$\Delta_t(t) = \left(\frac{1}{6f}\,|\ddot{f}|\,t^3\right) \quad (2)$$

where t is the duration of timing observations. We find $\Delta_t = 864$ s (230 cycles) over a time span of approximately 273 days. This is significantly larger than in other radio magnetars: ~120 s (22 cycles) over 277 days for XTE J1810–197 (Camilo et al. 2007c), ~124 s (60 cycles) over 6 months for 1E 1547.0–5408 (Camilo et al. 2008), and ~1080 s (250 cycles) over 20 months for PSR J1622–4950 (Levin et al. 2012). We note that these measurements were based only upon radio timing data, and included no X-ray TOAs. However, if we do not include the X-ray TOAs and instead restrict our analysis to the period covered by our phase-connected GBT observations, we find $\Delta_t = 140$ s (37 cycles) over a time span of approximately 167 days. This is closer to the level of timing noise observed in other radio magnetars.

The onset of the erratic state and the accompanying profile changes required a change in our timing analysis, as the simple standard template we used during the stable state was no longer adequate. We explored three options for obtaining TOAs: using the same three-component Gaussian template for all epochs, using a different Gaussian template for each epoch, and using a template based on the folded profiles at each epoch, but with noise removed using a wavelet smoothing algorithm. In the latter two cases, we attempted to align the different templates using the peak of the leading profile component as our reference point. We obtained TOAs using each method and attempted to extend the solution obtained during the stable state, but could not unambiguously maintain phase connection. We also tried to use a subset of TOAs from epochs just before the onset of the erratic state to establish a new solution without the need for many higher order frequency derivatives, and then to extend this simplified solution into the erratic state. Again, we could not unambiguously phase connect the data. Finally, we attempted to form a solution from only the TOAs obtained during the erratic state, as the magnetar could have experienced a glitch or other sudden change in rotational parameters, but we

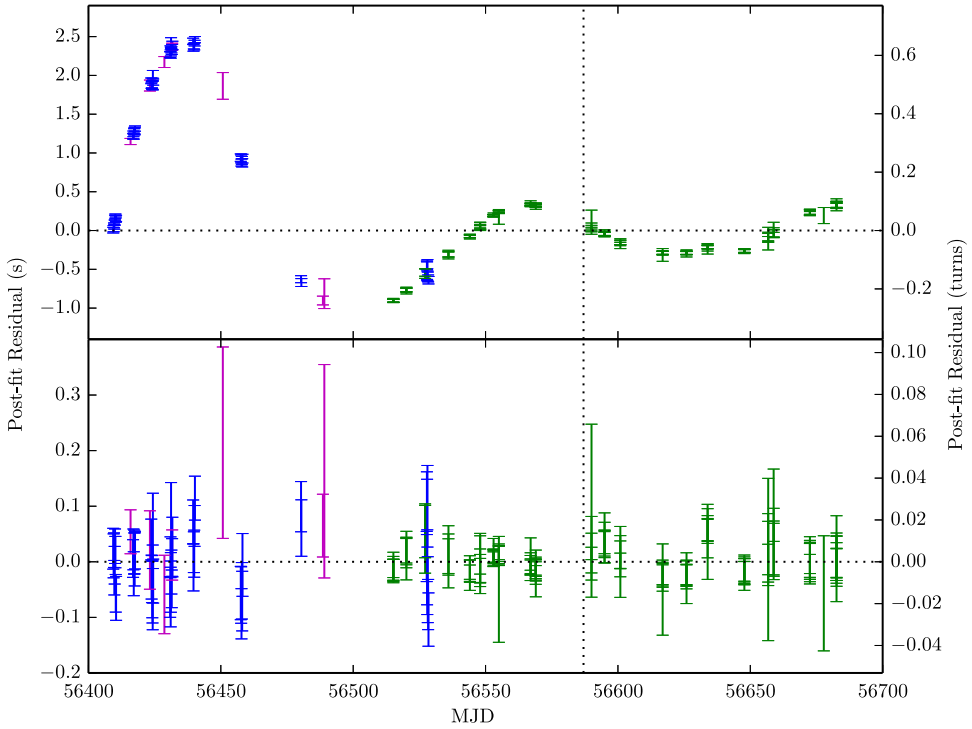

Figure 5. Post-fit timing residuals as a function of MJD. Only data from the stable state are shown here because we could not unambiguously phase connect data from the erratic state. TOAs from our GBT observations (green) are shown along with those previously published by Kaspi et al. (2014) from *Swift* (magenta) and *NuSTAR* (blue). The vertical dotted line indicates the reference epoch used in our timing model. The radio and X-ray TOAs are independently phase connected, with an arbitrary phase offset applied to align the two data sets. Top: the residual structure fitting only for f, $\dot{f}$, $\ddot{f}$, and $f^{(3)}$. The effects of timing noise are clearly evident. Bottom: the results of fitting for twelve frequency derivatives presented. Note the much smaller vertical scale.

still could not obtain a phase-connected solution. We are therefore unable to provide a precise timing solution for the erratic state. The implications of this are discussed in Section 5.

4.5. Single Radio Pulses

SGR J1745–2900 emits bright single radio pulses during most rotations. We analyzed the energy distribution, width, sub-pulse structure, and emission phase of the pulses.

4.5.1. Single Radio Pulse Energy Distribution

We identified single pulses by searching for peak fluxes whose maximum flux was ⩾4 times the off-pulse noise level. To avoid identifying noise spikes or microstructure in the single pulse as separate pulses, each single pulse was assigned its own on-pulse region using the same method as in Section 4.1, and the peak flux in this region was taken as representative of the entire single pulse. To limit contamination by RFI, we looked only for single pulses in the on-pulse region at this stage in the analysis (see Section 4.7 for an analysis at other pulse phases). Multiple sub-pulses in a single rotation were detected only about 30% of the time.

The single pulse fluxes at each epoch were normalized by the mean flux at that epoch. In Figure 6 we show two histograms, one for the energy distribution of all single pulses (gray) and one for only the brightest single pulse in a given rotation (hatched). Both distributions roughly follow a log-normal distribution. For all single pulses, the logarithmic mean is $\mu = -0.131$ and standard deviation $\sigma = 0.491$, and for the brightest single pulses $\mu = -0.145$ and $\sigma = 0.486$. There appears to be a high-energy tail to both observed, however. The log-normal approximation underestimates the observed number

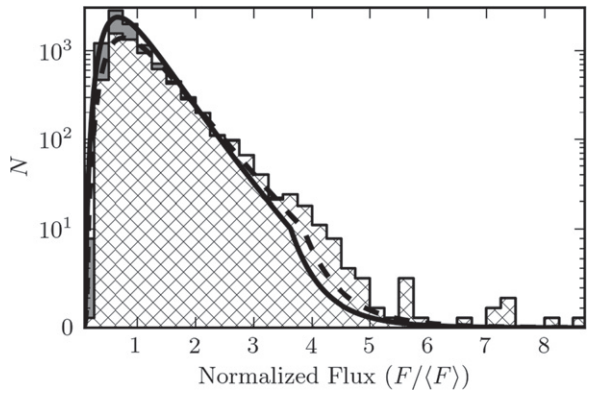

Figure 6. Histogram of peak single-pulse flux, normalized by the mean peak flux at that epoch. The hatched region shows only the brightest sub-pulse in a rotation, while the gray shaded region shows all sub-pulses in that rotation. The dashed line shows the best-fit log-normal distribution to the brightest pulses, and the solid line to all pulses, as described in the text. The presence of a high-energy tail is clearly visible above four times the mean flux. Note that the y-axis scaling changes from linear to logarithmic at values above 10.

of pulses at fluxes $F \gtrsim 3\langle F\rangle$, and especially at $F \gtrsim 4\langle F\rangle$. We note, though, that only about 1.6% of sub-pulses had $F \geqslant 3.0\langle F\rangle$. Levin et al. (2012) found that the single pulses of PSR J1622–4950 followed a log-normal distribution. A careful analysis of single pulses from XTE J1810–197 by Serylak et al. (2009) found a more complex distribution of single pulse energies, with emission sometimes best described by a combination of a power law and log-normal distribution because of the presence of a high-energy tail. In this regard, SGR J1745–2900 seems similar to XTE J1810–197.

4.5.2. Single Radio Pulse Widths

We characterized single pulse widths according to T_{90}, the time that encompassed 90% of the total pulse energy. This in turn was calculated as $T_{90} = T_{95} - T_5$, i.e., the times that encompassed 95% and 5% of the total pulse energy, respectively. The native time resolution of our raw data was 163.84 μs but this increased to ~3.7 ms in our folded and fully calibrated data. To maintain sensitivity to very narrow single pulse structure, we worked with de-dispersed time series retaining full time resolution data when measuring T_{90}, instead of the folded and calibrated data. We used the `PRESTO`[8] software suite (Ransom et al. 2002) to de-disperse the data at the DM of the magnetar, and used the accompanying `single_pulse_search.py` program to identify the times of individual pulses with S/N $\geqslant$ 5. This program identifies pulses by match-filtering the data with boxcar functions of various widths. We then identified the on-pulse region using the same technique as described in Section 4.1. We were then able to measure the integrated single pulse energy and calculate T_{90}.

Figure 7 shows a histogram of T_{90} for all of our observations (top panel), as well as for only the stable and erratic states (middle and bottom panels, repsectively). The shortest pulses had $T_{90} \approx 1$ ms, while the longest measured 23 ms. However, ~90% of pulses had $T_{90} < 4$ ms and ~99% had $T_{90} < 10$ ms. The mode of the distribution was 1.3 ms.

4.6. Single-pulse Differences Between the Stable and Erratic State

We performed the Kolmogorov–Smirnov (KS) test on the distribution of single pulse energies and T_{90} in the stable and erratic state. We found only a marginal difference in the single pulse energies when comparing all pulses (the null hypothesis is rejected at $p = 0.01$ level). However, we find significant evidence for a difference in the distribution of single pulse energies when considering only the brightestes single pulses in a rotation (at the $p = 2 \times 10^{-11}$ level) and in T_{90} (at the $p \sim 0$ level).

We hypothesized that the emergence of the third profile component was responsible for these differences. We tested this hypothesis by performing the KS test on the stable and erratic state, but only selecting pulses in the phase range of the main profile component. The results were similar, e.g., the KS test rejected the null hypothesis of identical T_{90} distributions at the $p = 1 \times 10^{-226}$ level.

The global properties of the T_{90} distribution are similar between the stable and erratic states, i.e., the modes (~1 ms), minima (~1 ms), and maxima ~23 ms) of the two distributions are nearly identical. The biggest differences are in the single pulse rate (1.538(6) s^{-1} in the stable state versus 0.381(4) s^{-1} in the erratic state) and the standard deviation (1.4 ms in the stable state versus 3 ms in the erratic state). The erratic state also has a higher fraction of pulses with $T_{90} > 5$ ms (see Figure 7).

4.6.1. Drifting Sub-pulses

We employed the 2D fluctuation spectrum method of Edwards & Stappers (2002) to search for and characterize any potential drifting sub-pulses. This method relies on a power

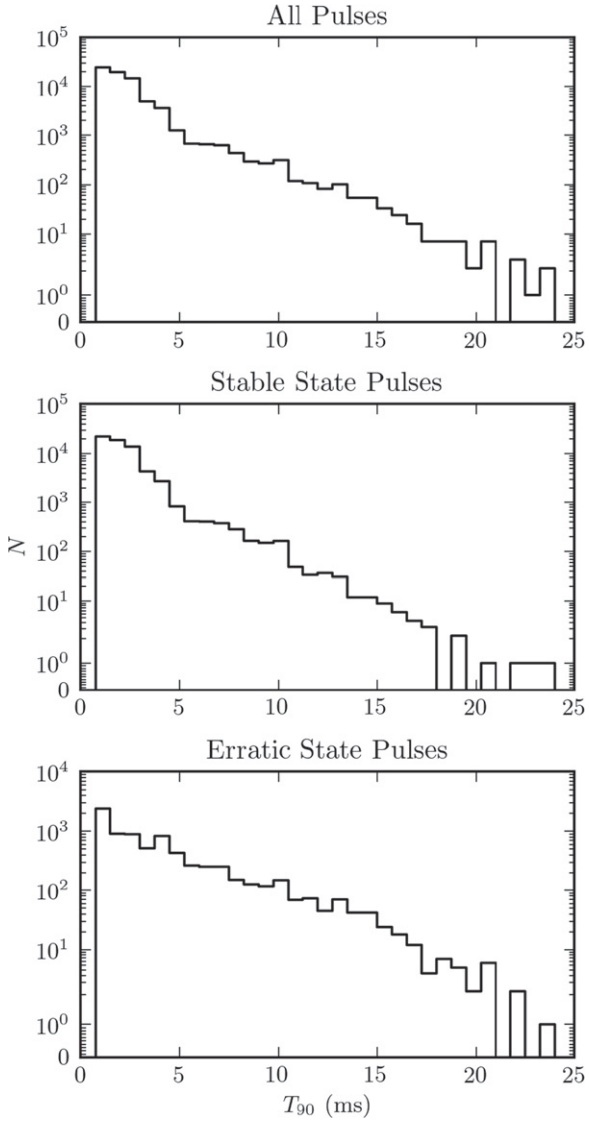

Figure 7. T_{90} of individual single pulses, as defined in the text. Top: distribution for pulses in both the stable and erratic state. The distribution is dominated by the much greater number of pulses in the stable state, especially at low T_{90}. Middle: distribution of pulses only in the stable state. Bottom: distribution of pulses only in the erratic state. There is a relative excess of pulses with $T_{90} > 5$ ms compared to the stable state. Note the change in y-axis scale.

spectrum of the 2D Fourier transform of pulse flux as a function of pulse phase and pulse number, i.e.,

$$S(u, v) = \left| \frac{1}{K} \sum_{j=0}^{n_{\rm bins}-1} \sum_{k=0}^{n_{\rm pulses}-1} F(j, k) e^{-2\pi i (uj+vk)} \right|^2, \quad (3)$$

where $K = n_{\rm bins} \times n_{\rm pulses}$ is a normalization factor (Lorimer & Kramer 2005). The signature of drifting sub-pulses is harmonic structure in $S(u, v)$, from which we can determine the characteristic spacing between sub-pulses and the period with which sub-pulses drift in phase.

The baseline fluctuations described in Section 3 caused significant red noise in u. There was sometimes an increase in power in v, but this was seen even when we only analyzed the off-pulse region (either in full or a randomly selected subset).

[8] http://www.cv.nrao.edu/~sransom/presto/

As such, we attribute it to an artifact of the data processing. We see no evidence for drifting sub-pulses in SGR J1745–2900.

4.7. Search for Off-pulse Radio Burst Emission

Some magnetars are observed to emit extremely bright X-ray bursts lasting ∼few ms. These bursts are sporadic and can occur at phases not typically associated with the on-pulse region. The magnetic reconnection model proposed by Lyutikov (2002) makes a clear prediction that such X-ray bursts should be accompanied by simultaneous radio bursts with very high fluxes. This model is particularly interesting in light of the recent discovery of a population of extremely bright, short duration radio bursts of apparently cosmological origin (Lorimer et al. 2007; Thornton et al. 2013; Spitler et al. 2014a). Unfortunately, we were unable to obtain simultaneous X-ray/radio observations of SGR J1745–2900, but we can still search for radio bursts that occur outside of the on-pulse region which, if detected, would suggest a possible link with the Lyutikov (2002) model and warrant further observations. For this analysis, we used tools in `PRESTO` and `single_pulse_search.py`. We de-dispersed the raw GBT data using an RFI mask generated by `PRESTO` at both the DM of the magnetar (1778 pc cm^{-3}) and at DM = 0 pc cm^{-3}, so that we could reject any remaining RFI. We then calculated the corresponding pulse phase of all single pulses with S/N $\geqslant$ 5, rejecting pulses that also appeared in the un-dispersed time series. No pulses were detected outside of the main pulse window. Of course, this does not rule out the Lyutikov (2002) model, since it may simply be the case that no X-ray bursts occurred during our observations.

5. DISCUSSION

SGR J1745–2900 is similar to other radio magnetars in many regards. It has a high degree of linear polarization, with a lower but significant fraction of circular polarization. It exhibits a high degree of timing noise. Its single pulse energy distribution is similar to that of XTE J1810–197. However, during the stable state it showed a level of radio flux density and profile stability not often seen in radio magnetars.

During the stable state, we observed a steady evolution in the separation between the two profile peaks. Prior to the start of our GBT observations, the profile was apparently single-peaked (Shannon & Johnston 2013; Spitler et al. 2014b). The growing separation between the peaks that we observed may suggest that the profile evolved smoothly from single to double peaked. However, the extended periods of minimal change in peak separation that we observed indicate that any such smooth change did not occur steadily. The emergence of the third profile component marked the onset of the erratic state, but there are hints of a widely separated component in some of the profiles presented by Eatough et al. (2013b) from MJDs 56414–56426. A joint analysis of both data sets could link this with the third component we observed. If this were the case it would raise the question of why the component remained dormant for many months before abruptly reappearing.

As noted in Section 4.6, the properties of the single pulse distribution changed between the stable and erratic states, most notably in T_{90}. This apparently cannot be explained, at least not entirely, by the emergence of the third profile component. Broadly speaking, whatever magnetospheric changes caused the onset of the erratic state also caused a decrease in the rate of single pulses while also producing a relative excess of single pulses with $T_{90} > 5$ ms.

Unlike the radio flux density, the X-ray flux has decayed mostly steadily since the initial outburst, although some short bursts have been detected with the *Swift* BAT (see Section 2). For comparison, the radio magnetar XTE J1810–197 faded in both the radio and X-ray bands following its discovery (Camilo et al. 2007c). The X-ray flux of 1E 1547–5408 decayed steadily following an outburst, while the radio flux density varied (Camilo et al. 2008). PSR J1622–4950 was discovered via its radio emission apparently during an X-ray outburst decay phase (Anderson et al. 2012), but it is not known exactly when the outburst started. After its radio discovery the flux of PSR J1622–4950 did decrease on a timescale of ∼700 days (Levin et al. 2012) but it is possible that it was fairly long-lived, and in this regard may be similar to SGR J1745–2900.

What caused SGR J1745–2900 to move into the erratic state? The change in mean flux and profile morphology suggests a significant reconfiguration of the magnetosphere. It would be useful to know if this was associated with a glitch or sudden change in spin-down, which is sometimes correlated with profile changes in other radio pulsars (Lyne et al. 2010). Unfortunately, our inability to maintain phase connection during this state prevents us from making such a definitive statement. We can speculate on the reasons for losing phase connection. One possibility is that the profile changes introduced too much uncertainty into the definition of a fiducial point in the profile to maintain phase connection. It is also possible that the gap between our observations was simply too large to maintain phase-coherence, given the uncertainties in the rotational parameters. We cannot rule this out, but we do note that the timing model presented by Kaspi et al. (2014) was accurate enough to maintain phase connection throughout the entire stable state, even before making any adjustments to the solution based on the radio data. Timing noise was clearly evident, but phase connection was maintained. The duration of the stable state was far greater than the ∼30 day gap between the observations over which we lost phase connection, and introducing an artificial ∼30 day gap in our data does not result in a loss of phase connection during the stable state. On the other hand, based on our analysis of timing noise presented in Section 4.4, SGR J1745–2900 exhibited a degree of timing noise unprecedented in radio magnetars when we included the time span covered by *NuSTAR* and *Swift* timing observations, though the reported timing noise values of other radio magnetars were based only on radio timing data. This timing noise was apparently large enough that it could also be interpreted as a sudden change in $\dot{f}$, possibly associated with an X-ray burst (Kaspi et al. 2014). Thus, there is precedent for timing noise in SGR J1745–2900 sufficient to introduce ambiguities in phase connected timing solutions. It is interesting to note, however, the coincidence between the radio variability and our inability to phase-connect, with both beginning roughly ∼300 days after the initial outburst. If our timing difficulties are not due to the gap or to the varying pulse profile, then this is reminiscent of behavior seen in magnetar 1E 1048.1–5937, in which, three times now, delayed torque variability followed an X-ray outburst after a ∼100 day decay (Archibald et al. 2015). In the latter case, radio emission is not seen, possibly due to unfavorable beaming. We speculate that we could therefore be seeing similar behavior in SGR J1745–2900, but with the additional radio diagnostic. Under

this scenario we would expect a relatively stable X-ray pulse profile for SGR J1745–2900 during the radio-variable phase. Unfortunately, we cannot verify this due to the low XRT PC-mode time resolution.

It is tempting to speculate that the increase in 44 GHz flux density (Yusef-Zadeh et al. 2014) is connected with the emergence of the third profile component. Unfortunately, the gap between the high frequency brightening and our closest observations prevent us from associating these events definitively. The measured flux of both observations that were taken closest to the 44 GHz brightening is not anomalously high, but we do see an eventual increase in $S_{8.7\,\mathrm{GHz}}$. This suggests that the 44 GHz brightening was not long-lived, but may be associated with greater variability in flux overall.

The literature does not contain reports of similar state changes in the other radio magnetars, so it is possible that SGR J1745–2900 is unique in this regard. However, most of the published data on the other radio magnetars were collected shortly after they underwent an X-ray outburst and subsequent radio brightening. It would be interesting to search for a switch to a stable state in other sources on long time scales, and perhaps a return to an erratic state.

6. CONCLUSIONS

We observed the magnetar SGR J1745–2900 for 11 months starting in 2013 August using the GBT, measuring its radio flux density, pulse profile shape, single-pulse behavior, and timing parameters. We have also analyzed publicly available *Swift* XRT data from the initial outburst of the magnetar, tracking its X-ray flux and spectral evolution. We find that for the first 5.5 months of our GBT observations, the radio flux density and pulse profile remained relatively stable, with a slow increase in the pulse width and separation between two profile peaks. This is in contrast to the three other radio magnetars, which were all highly variable in the radio band. During this time, the magnetar exhibited a high degree of timing noise but did not otherwise experience any anomalous rotational behavior. After this stable period, SGR J1745–2900 entered an erratic state around 2014 March marked by a higher and more variable radio flux density and significant changes in the radio pulse profile from epoch to epoch, as well as changes in the single pulse behavior. We were unable to maintain phase connection, but can only speculate as to the causes. The onset of this erratic state occurred within two weeks of a short-lived increase in radio density at 44 GHz measured with the VLA (Yusef-Zadeh et al. 2014). The X-ray flux of SGR J1745–2900 has steadily decayed since the initial outburst, and did not deviate from this trend at any point during the time span covered by our GBT observations, including during the erratic radio state. We conclude that whatever caused the erratic radio state is decoupled from the X-ray emission.

The authors wish to thank Paul Demorest for invaluable assistance in processing the GBT data, and for helping to track down and correct some instrumental and hardware errors. We also thank an anonymous referee for value suggestions that improved our analysis. The National Radio Astronomy Observatory is a facility of the National Science Foundation operated under cooperative agreement by Associated Universities, Inc. We acknowledge the use of public data from the *Swift* data archive. This research made use of the XRT Data Analysis Software (XRTDAS) developed under the responsibility of the ASI Science Data Center (ASDC, Italy). The *NuSTAR* mission is a project led by the California Institute of Technology, managed by the Jet Propulsion Laboratory, and funded by the National Aeronautics and Space Administration. This research made use of the NuSTAR Data Analysis Software (NuSTARDAS) jointly developed by ASDC and the California Institute of Technology. V. K. receives support from an NSERC Discovery Grant and Accelerator Supplement, from the Centre de Recherche en Astrophysique du Québec, an R. Howard Webster Foundation Fellowship from the Canadian Institute for Advanced Study, the Canada Research Chairs Program, and the Lorne Trottier Chair in Astrophysics and Cosmology. R.A. receives support from a Walter C. Sumner Memorial Fellowship.

REFERENCES

Anderson, G. E., Gaensler, B. M., Slane, P. O., et al. 2012, ApJ, 751, 53
Archibald, R. F., Kaspi, V. M., Ng, C.-Y., et al. 2015, ApJ, 800, 33
Arzoumanian, Z., Nice, D. J., Taylor, J. H., & Thorsett, S. E. 1994, ApJ, 422, 671
Bates, S. D., Lorimer, D. R., & Verbiest, J. P. W. 2013, MNRAS, 431, 1352
Beloborodov, A. M. 2009, ApJ, 703, 1044
Burrows, D. N., Hill, J. E., Nousek, J. A., et al. 2005, SSRv, 120, 165
Camilo, F., Cognard, I., Ransom, S. M., et al. 2007c, ApJ, 663, 497
Camilo, F., Ransom, S. M., Halpern, J. P., & Reynolds, J. 2007a, ApJL, 666, L93
Camilo, F., Ransom, S. M., Halpern, J. P., et al. 2006, Natur, 442, 892
Camilo, F., Ransom, S. M., Peñalver, J., et al. 2007d, ApJ, 669, 561
Camilo, F., Reynolds, J., Johnston, S., Halpern, J. P., & Ransom, S. M. 2008, ApJ, 679, 681
Camilo, F., Reynolds, J., Johnston, S., et al. 2007b, ApJL, 659, L37
Degenaar, N., Miller, J. M., Kennea, J., et al. 2013, ApJ, 769, 155
Degenaar, N., Reynolds, M., Miller, J., et al. 2014, ATel, 6458, 1
Dib, R., & Kaspi, V. M. 2014, ApJ, 784, 37
Eatough, R., Karuppusamy, R., Champion, D., et al. 2013a, ATel, 5058, 1
Eatough, R. P., Falcke, H., Karuppusamy, R., et al. 2013b, Natur, 501, 391
Edwards, R. T., & Stappers, B. W. 2002, A&A, 393, 733
Ferdman, R. D., Stairs, I. H., Kramer, M., et al. 2013, ApJ, 767, 85
Gavriil, F. P., & Kaspi, V. M. 2002, ApJ, 567, 1067
Hotan, A. W., van Straten, W., & Manchester, R. N. 2004, PASA, 21, 302
Kaspi, V. M., Archibald, R. F., Bhalerao, V., et al. 2014, ApJ, 786, 84
Kennea, J. A., Burrows, D. N., Cummings, J., et al. 2013a, ATel, 5124, 1
Kennea, J. A., Burrows, D. N., Cummings, J., et al. 2013b, ATel, 5254, 1
Kennea, J. A., Burrows, D. N., Kouveliotou, C., et al. 2013c, ApJL, 770, L24
Kennea, J. A., Krimm, H., Barthelmy, S., et al. 2013d, ATel, 5009, 1
Kramer, M., Stappers, B. W., Jessner, A., Lyne, A. G., & Jordan, C. A. 2007, MNRAS, 377, 107
Levin, L., Bailes, M., Bates, S., et al. 2010, ApJL, 721, L33
Levin, L., Bailes, M., Bates, S. D., et al. 2012, MNRAS, 422, 2489
Lorimer, D. R., Bailes, M., McLaughlin, M. A., Narkevic, D. J., & Crawford, F. 2007, Sci, 318, 777
Lorimer, D. R., & Kramer, M. 2005, in Handbook of Pulsar Astronomy, ed. R. Ellis et al. (Cambridge: Cambridge Univ. Press), 187
Lyne, A., Hobbs, G., Kramer, M., Stairs, I., & Stappers, B. 2010, Sci, 329, 408
Lyutikov, M. 2002, ApJL, 580, L65
Mereghetti, S., Gotz, D., Ferrigno, C., et al. 2013, GCN, 15236, 1
Mori, K., Gotthelf, E. V., Zhang, S., et al. 2013, ApJL, 770, L23
Olausen, S. A., & Kaspi, V. M. 2014, ApJS, 212, 6
Ransom, S. M., Eikenberry, S. S., & Middleditch, J. 2002, AJ, 124, 1788
Rea, N., Esposito, P., Pons, J. A., et al. 2013, ApJL, 775, L34
Rea, N., Haggard, D., Baganoff, F., et al. 2014, ATel, 5922, 1
Serylak, M., Stappers, B. W., Weltevrede, P., et al. 2009, MNRAS, 394, 295
Shannon, R. M., & Johnston, S. 2013, MNRAS, 435, L29
Spitler, L. G., Cordes, J. M., Hessels, J. W. T., et al. 2014a, ApJ, 790, 101
Spitler, L. G., Lee, K. J., Eatough, R. P., et al. 2014b, ApJL, 780, L3
Taylor, J. H. 1992, RSPTA, 341, 117
Thompson, C., & Duncan, R. C. 1995, MNRAS, 275, 255
Thompson, C., & Duncan, R. C. 1996, ApJ, 473, 322
Thompson, C., Lyutikov, M., & Kulkarni, S. R. 2002, ApJ, 574, 332
Thornton, D., Stappers, B., Bailes, M., et al. 2013, Sci, 341, 53
Verner, D. A., Ferland, G. J., Korista, K. T., & Yakovlev, D. G. 1996, ApJ, 465, 487
Wilms, J., Allen, A., & McCray, R. 2000, ApJ, 542, 914
Yusef-Zadeh, F., Roberts, D., Heinke, C., et al. 2014, ATel, 6041, 1